

Global collapse of molecular clouds as a formation mechanism for the most massive stars

N. Peretto^{1,2}, G. A. Fuller^{3,4}, A. Duarte-Cabral^{5,6}, A. Avison^{3,4}, P. Hennebelle², J. E. Pineda^{3,4,7}, Ph. André², S. Bontemps^{5,6}, F. Motte², N. Schneider^{5,6}, S. Molinari⁸

¹ School of Physics and Astronomy, Cardiff University, Queens Buildings, The Parade, Cardiff CF24 3AA, UK
e-mail: Nicolas.Peretto@astro.cf.ac.uk

² Laboratoire AIM, CEA/DSM-CNRS-Université Paris Diderot, IRFU/Service d'Astrophysique, C.E. Saclay, France

³ Jodrell Bank Centre for Astrophysics, School of Physics and Astronomy, University of Manchester, Manchester, M13 9PL, UK

⁴ UK ALMA Regional Centre node

⁵ Université de Bordeaux, LAB, UMR5804, F-33270, Floirac, France

⁶ CNRS, LAB, UMR5804, F-33270, Floirac, France

⁷ European Southern Observatory (ESO), Garching, Germany

⁸ IFSI, INAF, Area di Ricerca di Tor Vergata, Via Fosso Cavaliere 100, I-00133, Roma, Italy

Received;accepted

ABSTRACT

The relative importance of primordial molecular cloud fragmentation and large-scale accretion still remains to be assessed in the context of massive core/star formation. Studying the kinematics of dense gas surrounding massive star progenitors can tell us if large-scale flow of material impact the mass growth of massive star forming cores. Here we present a comprehensive dataset, including Atacama Large Millimeter Array (ALMA) Cycle 0 observations, of the 5500(\pm 800) M_{\odot} Infrared Dark Cloud SDC335.579-0.272 (hereafter SDC335) which exhibits a network of cold, dense, parsec-long filaments. ALMA reveals the presence of two massive star forming cores, one of which contains 545($^{+770}_{-385}$) M_{\odot} of gas within ~ 0.05 pc, seating at the centre of SDC335 where filaments intersect. ALMA and Mopra single dish observations of the SDC335 dense gas reveal that the kinematics of this hub-filament system is consistent with a global collapse of the cloud. These molecular line data point towards an infall velocity $V_{infall} = 0.7(\pm 0.2)$ km/s, and a total mass infall rate $\dot{M}_{infall} \approx 2.5(\pm 1.0) \times 10^{-3} M_{\odot} \text{ yr}^{-1}$ towards the central pc-size region of SDC335. **Such an infall rate brings 750(\pm 300) M_{\odot} of gas to the centre of the cloud per free-fall time ($t_{ff} = 3 \times 10^4$ yr). This is enough to double the mass already present in the central pc-size region in $3.5^{+2.2}_{-1.0} \times t_{ff}$. All indicates that thanks to the global collapse of SDC335 enough mass has been gathered at its centre during the past million year allowing for the formation of an early O-type star progenitor.**

Key words. star formation - kinematics

1. Introduction

The formation of massive stars remains, in many ways, a mystery (Beuther et al. 2007; Zinnecker & Yorke 2007). More specifically, the key question of what physical processes determine their mass accretion history is yet to be answered. On one hand, some theories predict that primordial fragmentation of *globally stable* molecular clouds may form compact reservoirs of gas, called cores (with sizes up to 0.1pc), from which a forming star *subsequently* accumulates its mass (McKee & Tan 2003; Beuther & Schilke 2004). In an alternative scenario, molecular clouds *undergo global* collapse (Peretto et al. 2006, 2007), gathering matter from large scales to the centre of their gravitational potential well, where cores, and protostars in them, are *simultaneously* growing in mass (Bonnell et al. 2004; Smith et al. 2009). **Only detailed observations of individual massive star forming cloud can provide hints on which of these scenarios, if any, is most relevant.**

The cloud under investigation is the *Spitzer Dark Cloud* SDC335.579-0.292 (hereafter SDC335; Peretto & Fuller 2009), a massive infrared dark cloud (IRDC) located at a distance of 3.25 kpc from the Sun (obtained using the Reid et al. (2009) model). The low level of radiative feedback from protostars

in IRDCs ensures that the initial conditions for star formation are still imprinted in the gas properties (Rathborne et al. 2006; Peretto & Fuller 2010). Massive IRDCs, such as SDC335, are therefore ideal places to study the earliest stages of high-mass star formation (e.g. Kauffmann & Pillai 2010). SDC335 exhibits a remarkable network of filaments seen in extinction at $8\mu\text{m}$ (Fig. 1), reminiscent of hub-filament systems (Myers 2009) observed in a number of low-mass (André et al. 2010; Peretto et al. 2012) and high-mass (Schneider et al. 2012; Hennemann et al. 2012) star-forming regions. The SDC335 filaments intersect at the centre of the cloud where two infrared protostars ($L_{bol} > 2 \times 10^4 L_{\odot}$; Garay et al. 2002) excite extended $4.5\mu\text{m}$ emission, a tracer of powerful outflow activity (Cyganowski et al. 2008). Consistently, class II methanol masers, unique tracers of massive star formation (Xu et al. 2008), have also been reported towards these sources (Caswell et al. 2011). However, despite these signposts of massive star formation, no 6cm free-free emission has been detected towards SDC335 down to a limit of 0.2 mJy (Garay et al. 2002). This shows that little gas has been ionized in the centre of SDC335 and suggests that we are witnessing the early stages of the formation of, at least, two massive stars.

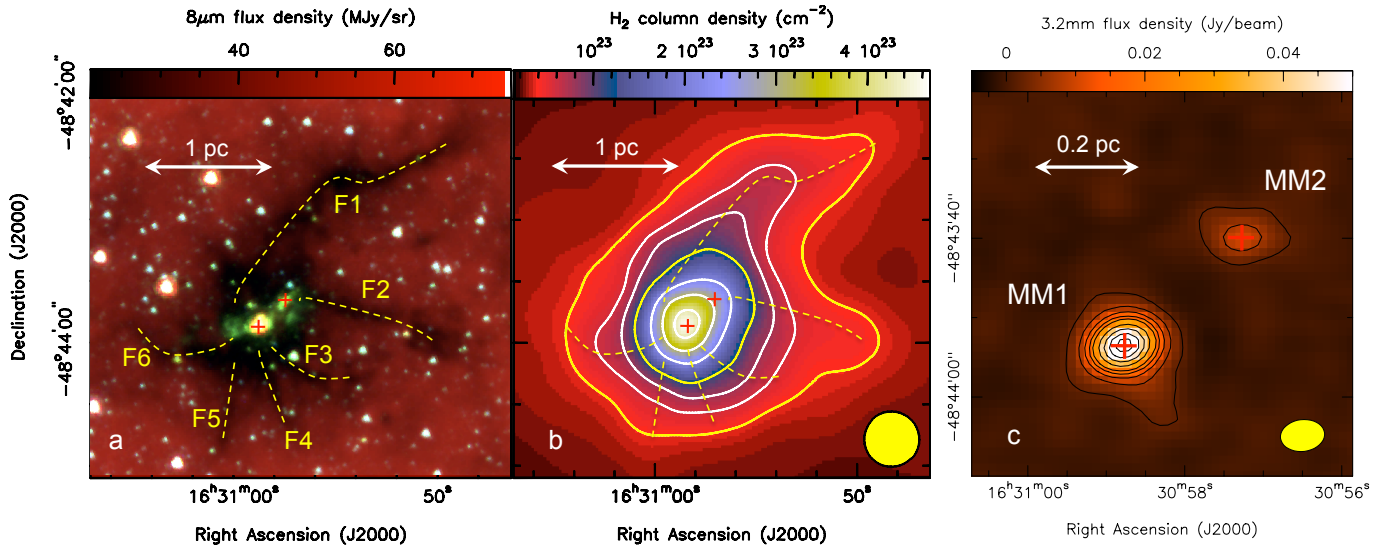


Fig. 1. (a) Mid-infrared *Spitzer* composite image (red: $8\mu\text{m}$; green: $4.5\mu\text{m}$; blue: $3.6\mu\text{m}$) of SDC335. The 6 filaments identified by eye are enhanced with yellow dashed lines, emphasizing their converging pattern. The diffuse $4.5\mu\text{m}$ emission associated with the two IR sources in the centre is usually interpreted as a signature of powerful outflow activity. The positions of the two cores are marked with red crosses. (b) *Herschel* column density image of SDC335. The locations of filaments and cores are marked similarly as in the (a) panel. The final angular resolution of this image is $25''$ (yellow circle), that of *Herschel* at $350\mu\text{m}$ (see text). The contours go from 3.5×10^{22} to 9.5×10^{22} in steps of 2×10^{22} cm^{-2} , and from 1.15×10^{23} to 4.15×10^{23} cm^{-2} in steps of 1×10^{23} cm^{-2} . The two yellow contours define the regions in which we calculated the SDC335 and Centre masses quoted in Table 1. (c) ALMA 3.2mm dust continuum emission of the central region of SDC335 where two cores are identified, MM1 and MM2. The rms noise is 0.4 mJy/beam. The contours go from 2 to 22 in steps of 5 mJy/beam, and from 22 to 62 in steps of 10 mJy/beam. The yellow ellipse represents the ALMA beam size.

The goal of this paper is to map the dense gas kinematics of SDC335 and analyze it in the context of massive star formation scenarios. In Section 2 we describe the observations. In Section 3 we discuss the mass partition in SDC335, and Section 4 presents observations of the SDC335 dense gas kinematics. Finally, we discuss our results and their implications in Section 5, summary and conclusions are presented in Section 6.

2. Observations

2.1. *Spitzer* and *Herschel* observations

In this paper we make use of publicly available¹ *Spitzer* GLIMPSE data (Churchwell et al. 2009). The angular resolution of the $8\mu\text{m}$ data is $\sim 2''$. We also make use of the PACS (Poglitsch et al. 2010) $160\mu\text{m}$ and SPIRE (Griffin et al. 2010) $350\mu\text{m}$ *Herschel* (Pilbratt et al. 2010) data from the Hi-GAL survey (Molinari et al. 2010). These data were reduced as described in Traficante et al. (2011), using the ROMAGAL map making algorithm. The nominal angular resolution at these two wavelengths are $12''$ and $25''$.

2.2. Mopra observations

In May 2010 we observed SDC335 with the ATNF Mopra 22m single dish telescope. We observed transitions such as $\text{HCO}^+(1-0)$, $\text{H}^{13}\text{CO}^+(1-0)$ and $\text{N}_2\text{H}^+(1-0)$ in a $5' \times 5'$ field centered on SDC335. We performed on-the-fly observations, switching to an off position free of dense gas emission. Pointing was checked every hour and was found to be better than $10''$. We used the zoom mode of the MOPS spectrometer providing a velocity resolution of 0.1 km/s. The angular resolution of these 3mm Mopra

observation is $\sim 37''$ and the rms noise is 0.1 K in T_A^* scale (~ 0.2 K in T_{mb} scale).

2.3. ALMA observations

In September and November 2011 we observed SDC335 at 3mm wavelength with the 16 antennas of the ALMA (Cycle 0) interferometer in its compact configuration. We performed an 11 pointing mosaic covering the entire area seen in extinction with *Spitzer* (Fig. 1a). We simultaneously observed the 3.2mm dust continuum, along with the $\text{CH}_3\text{OH}(13-12)$ and $\text{N}_2\text{H}^+(1-0)$ transitions at a spectral resolution of ~ 0.1 km/s. Flux and phase calibration were performed on Neptune and B1600-445, respectively. The data have been reduced using CASA² (McMullin et al. 2007). The synthesized beam is $5.6'' \times 4.0''$ with a position angle of $+97^\circ$. The rms noise in the continuum is 0.4 mJy/beam, while for line we reach a rms sensitivity of 14 mJy/beam (~ 0.08 K).

As with any interferometer, ALMA filters out large scale emission. In order to recover this emission, we have used the Mopra single dish data to provide the short-spacing information. We did this using the GILDAS³ software. In particular this combination significantly improved the image quality in the central region of SDC335. The rms noise on these combined datacube is 0.14 Jy/beam (~ 0.8 K), significantly larger than the ALMA-only dataset. This reflects the higher noise of the Mopra dataset **per ALMA beam**.

3. Mass partition in SDC335

The mid-infrared composite image of SDC335 is displayed in Fig. 1a. In extinction we easily identify a network of 6 filaments

² <http://casa.nrao.edu>

³ <http://www.iram.fr/IRAMFR/GILDAS>

¹ <http://irsa.ipac.caltech.edu/data/SPITZER/GLIMPSE>

Table 1. Mass partition in SDC335. **Sizes are all beam-deconvolved, and refer either to diameters when spherical geometry is assumed, or to diameters \times lengths when cylindrical geometry is assumed.**

Structure name	Sizes (pc)	Mass (M_{\odot})	Volume density (cm^{-3})
SDC335	2.4	$5.5(\pm 0.8) \times 10^3$	$1.3(\pm 0.2) \times 10^4$
Centre	1.2	$2.6(\pm 0.3) \times 10^3$	$5.0(\pm 0.6) \times 10^4$
F1	0.3×2.0	$0.4(\pm 0.1) \times 10^3$	$4.9(\pm 1.3) \times 10^4$
F2	0.3×1.3	$0.2(\pm 0.1) \times 10^3$	$3.7(\pm 1.8) \times 10^4$
MM1	0.054	$545^{(+770)}_{(-385)}$	$1.1^{(+1.7)}_{(-0.8)} \times 10^8$
MM2	0.057	$65^{(+92)}_{(-46)}$	$1.2^{(+1.6)}_{(-0.9)} \times 10^7$

(enhanced as yellow dashed lines, and named F1 to F6), while in the centre of SDC335 we observe the presence of bright infrared sources exciting diffuse $4.5\mu\text{m}$ emission (in green). In the following we provide mass measurements of the entire SDC335 clump, the filaments, and the cores at the centre.

3.1. Clump and filaments

Mid-infrared extinction mapping of IRDCs is a powerful method to measure their column density distribution at high resolution (Peretto & Fuller 2009; Butler & Tan 2009). From the resulting maps one can measure the masses of these clouds. However, this method is limited, by definition, to mid-infrared absorbing dust, and in cases such as SDC335, where bright $8\mu\text{m}$ sources have already formed, the resulting dust extinction masses become more uncertain. Using *Herschel* data allows us to circumvent this issue by looking at far-infrared dust emission from $70\mu\text{m}$ up to $500\mu\text{m}$. A standard way for recovering the column density distribution from *Herschel* data is to perform a pixel-by-pixel SED fitting after smoothing the data to the *Herschel* $500\mu\text{m}$ resolution ($36''$). In order to get better angular resolution, we decided here to use the $160\mu\text{m}/350\mu\text{m}$ ratio map⁴ of SDC335 as an indicator of the dust temperature, and then reconstruct the column density distribution at $25''$ resolution by combining the dust temperature (T_d) and $350\mu\text{m}$ (S_{350}) maps assuming that dust radiates as a modified black-body. The column density is therefore written as:

$$N_{H_2}(x, y) = S_{350}(x, y) / [B_{350}(T_d(x, y)) \kappa_{350} \mu m_H] \quad (1)$$

where B_{350} is the Planck function measured at $350\mu\text{m}$, $\mu = 2.33$ is the average molecular weight, m_H is the atomic mass of hydrogen, and κ_{350} is the specific dust opacity at $350\mu\text{m}$. Using the following dust opacity law (Hildebrand 1983; Beckwith et al. 1990) $\kappa_{\lambda} = 0.1 \times \left(\frac{\lambda}{0.3\text{mm}}\right)^{-\beta} \text{cm}^2\text{g}^{-1}$ with $\beta = 2$, we constructed the SDC335 column density map presented in Fig. 1b. We can see that, despite the lower resolution, the column density structure of SDC335 follows the extinction features we see in mid-infrared. We can also notice that the entire central pc-size region lies above a high column density of $1 \times 10^{23} \text{cm}^{-2}$.

The dust opacity parameters we used to construct the SDC335 column density map are rather uncertain. There are indications (e.g. Paradis et al. 2010) that for cold, dense clouds a spectral index $\beta \approx 2.4$ is possibly more adapted. The net effect of using a lower β is to overestimate the temperature, and therefore underestimate the column density (and the mass calculated from this column density). Also, the dust emission towards

IRDCs is composed of the emission from the the cloud itself and emission from the galactic plane background/foreground dust which is warmer and more diffuse. A consequence of this is that, once again, the IRDC temperature we calculate is overestimated. The measured average dust temperature towards the coldest parts of SDC335 is $\sim 16 \text{K}$ (see Fig. A.1) which appears to be, indeed, 2-3 K warmer compared to other IRDCs (Peretto et al. 2010). Altogether, the column densities presented in Fig. 1b are likely to be underestimated. In order to get an upper limit on the SDC335 column density we decreased the dust temperature map by 2 K, which brings back SDC335 in the typical temperature range observed in IRDCs. We then recalculated the column density map using Eq. (1). Masses and uncertainties quoted in Table 1 for SDC335, the Centre region, the F1 and F2 filaments have been obtained taking the average mass obtained from the two *Herschel* column density maps. All masses are background-subtracted, which correspond, for a centrally concentrated source, to the mass enclosed in a specific column density contour. For SDC335 and the Centre regions, the sizes correspond to the diameter of the disc having the same areas, for F1 and F2 they correspond to the two dimensions of the rectangle having the same areas. The surface areas of these two filaments correspond to polygon areas we drew on the *Herschel* column density map around the F1 and F2 filaments. The widths of these polygons are constrained by the filament profiles as seen in the $8\mu\text{m}$ extinction map ($4''$ resolution), and which correspond to $\sim 0.3 \text{pc}$. Note that for the filaments we performed an independent mass measurement directly using the $8\mu\text{m}$ extinction map from Peretto & Fuller (2009), confirming the *Herschel* mass measurements. Densities are then calculated assuming spherical geometry for SDC335 and Centre regions, cylindrical geometry for the F1 and F2 filaments.

3.2. Dense cores

The ALMA 3.2mm dust continuum observations presented in Fig. 1c show the presence of two bright sources, MM1 and MM2, which J2000 coordinates are (RA: $16^{\text{h}}30^{\text{m}}58.76^{\text{s}}$; Dec: $-48^{\circ}43'53.4''$) and (RA: $16^{\text{h}}30^{\text{m}}57.26^{\text{s}}$; Dec: $-48^{\circ}43'39.7''$), respectively. Each of these cores is associated with one infrared source and one class II methanol maser (Caswell et al. 2011), leaving no doubt that MM1 and MM2 are currently forming massive stars.

The MM1 and MM2 cores are compact but partially resolved. The results of a 2D Gaussian fit to the 3.2mm continuum emission of these compact sources give integrated fluxes of $101(\pm 10) \text{mJy}$ and $12(\pm 2) \text{mJy}$ and deconvolved sizes of 0.054pc and 0.057pc , for MM1 and MM2 respectively. To estimate how much of this emission could be free-free, we took the $3\text{-}\sigma$ non-detection limit at 6cm from Garay et al. (2002) and scaled it to 3.2mm using $F_{\text{ff}}^{\lambda} = 0.2 \text{mJy} \times [60/\lambda(\text{mm})]^{\alpha}$. Upper limits on α have been determined for a set of massive protostellar objects and HCHII regions (Cyganowski et al. 2011; Hoare 2005) consistent with $\alpha = 1.5$. This provides an upper limit for free-free contamination at 3.2mm of $F_{\text{ff}}^{3.2} = 4 \text{mJy}$. Clearly this is negligible for MM1, whereas it could contribute up to 33% of the MM2 flux. **In the strict upper case limit of an optically thick free-free emission α equals 2. However, the recent detection of MM1 at 7mm with ATCA (Avison et al. in prep.) constrains the range of free-free contamination between 0%**

⁴ Note that we did not use the $250\mu\text{m}$ image because of the significant fraction of saturated pixels at the centre of SDC335.

⁵ Note that in the same study the authors also determine, for one source, a lower limit of $\alpha > 1.7$, but this measurement is based on a single 4.2σ detection of a very weak source.

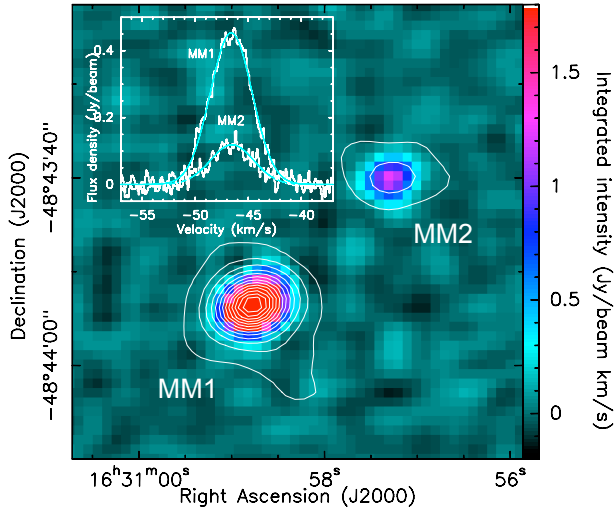


Fig. 2. ALMA CH₃OH(13-12) integrated intensity image of SDC335 in colour scale, overplotted are the contours of the 3.2mm dust continuum emission as displayed in Fig. 1c. We can see that both types of emission spatially coincide. The insert on the top left corner shows the methanol spectra observed at the central position of each core. The cyan solid lines are the best Gaussian fit to the data.

and 33% of the ALMA 3.2mm flux, depending on the exact value of the spectral index β used for the MM1 SED fitting. A contamination of 33% will not change any of the results presented in this paper, therefore we neglect any potential free-free contamination in the remainder of the paper. The gas mass and the 3.2mm flux of the MM cores are related through

$$M_{gas} = \frac{d^2 F_{3.2}}{\kappa_{3.2} B_{3.2}(T_d)} \quad (2)$$

where d is the distance to the source, $F_{3.2}$ is the 3.2mm flux, $\kappa_{3.2}$ is the specific dust opacity (accounting for the dust to gas mass ratio) and $B_{3.2}(T_d)$ is the Planck function measured at 3.2mm with a dust temperature T_d . The main sources of uncertainties on this mass estimate come from the dust properties, temperature and opacity. The dust temperature of these two sources are difficult to determine based on these ALMA observations alone. However both sources have strong mid/far-IR emission seen with *Spitzer* (Churchwell et al. 2009) and *Herschel* (Molinari et al. 2010), class II methanol maser emission (Caswell et al. 2011) and are detected in high excitation thermal lines of methanol (Sec. 4). These are indicative of dust in the centre of the cores with temperatures > 100 K, but it is also clear that on larger scales, the dust within the dark SDC335 filaments is cold, with temperatures ~ 15 K as measured in many other IRDCs (Peretto et al. 2010; Wilcock et al. 2012). For the vast majority of massive protostellar cores in the literature (cf caption of Fig. 6), the assumed or measured dust/gas temperature (via SED or K-ladder fitting of some specific lines) varies between 15 K and 100 K. Here, we adopt an intermediate dust temperature of 50 K for both MM cores, considering that a factor of 2 uncertainty on this dust temperature is conservative. In the future, radiative transfer modelling of these sources will be necessary to better constrain their temperature profiles.

We take the same dust opacity law as used for the *Herschel* data, providing $\kappa_{3.2} = 8.7 \times 10^{-4} \text{ cm}^2 \text{ g}^{-1}$ (assuming a dust to gas mass ratio of 1%). However, this value is sensitive to the dust model used. It is unclear which model is the most appropriate for protostellar cores, but as shown in Fig. 6, most values adopted

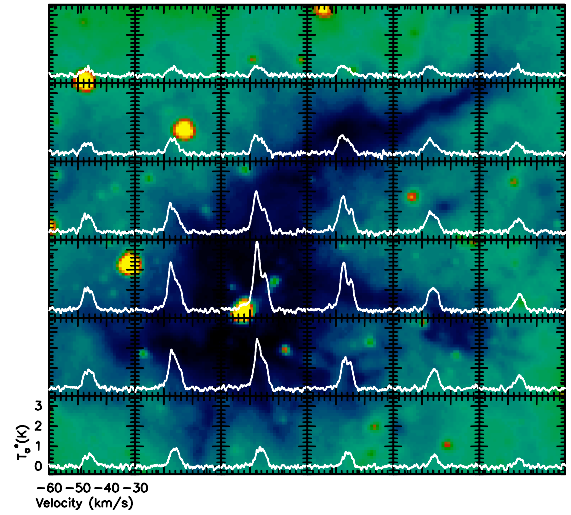


Fig. 3. *Spitzer* 8 μ m image of SDC335 (colour scale) over-plotted with the Mopra HCO⁺(1-0) spectra. The temperature scale and velocity are indicated in the bottom left corner. The HCO⁺(1-0) line is self-absorbed and blue-shifted in the bulk of the cloud. This is usually interpreted as a signature of collapse.

in the literature for core mass measurements agree within a factor of 2. With these assumptions we estimate the gas masses and their associated uncertainties as $M_{MM1} = 545^{+770}_{-385} M_{\odot}$ and $M_{MM2} = 65^{+92}_{-46} M_{\odot}$.

4. Dense gas kinematics in SDC335

In this section we discuss the dense gas kinematics of the cores, filaments and clump as observed with the Mopra and ALMA telescopes.

4.1. ALMA CH₃OH(13-12) core velocities

In order to determine the systemic velocity of the MM cores, we mapped the thermal methanol CH₃OH(13-12) transition at 105.063761 GHz. Due to the high energy levels of this transition ($E_u = 223.8$ K), CH₃OH(13-12) is preferentially observed in dense and warm regions. Figure 2 shows the ALMA integrated intensity image towards the cores. We see the excellent agreement between the position of the peak of the dust continuum cores and the methanol emission, indicating that methanol is a good tracer of their systemic velocities. We also note that the methanol emission is more compact (unresolved, **i.e.** < 0.01 pc) than the dust continuum emission which indicates that it arises from the warm, innermost regions of the cores. Gaussian fits to the methanol spectra observed at the central position of the two cores (insert of Fig. 2) provide the systemic velocities of the cores ($V_{MM1} = -46.6$ km/s, $V_{MM2} = -46.5$ km/s) and the gas velocity dispersion in the densest parts of MM1 and MM2 ($\Delta V_{MM1} = 4.6$ km/s, $\Delta V_{MM2} = 4.8$ km/s).

4.2. Mopra HCO⁺(1-0) self-absorbed lines

HCO⁺ is a well known tracer of dense gas in molecular clouds. In these regions, HCO⁺(1-0) can be optically thick, in which case the line shape can provide information of the global motions of the gas along the line of sight (e.g. Fuller et al. 2005; Smith et al. 2012). The HCO⁺(1-0) observations towards SDC335 (Fig. 3) show blue-shifted self-absorbed spectra in the

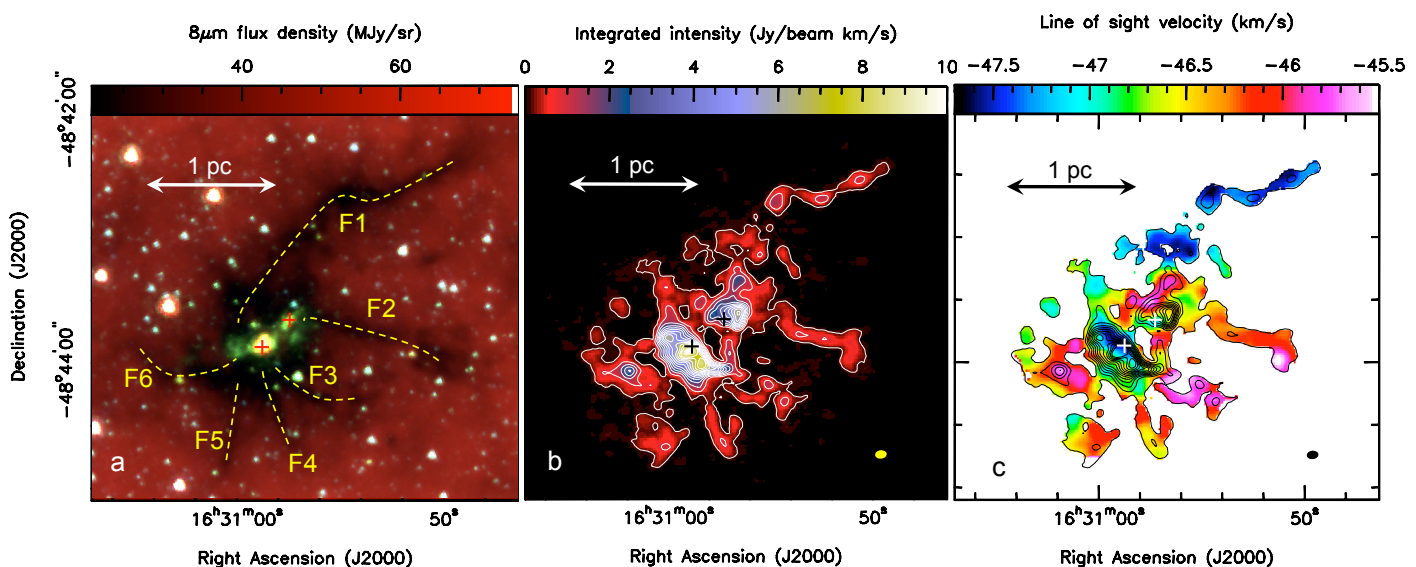


Fig. 4. (a) Same as in Fig. 1a; (b) ALMA-only image of the $N_2H^+(1-0)$ integrated intensity over the 7 hyperfine structure components. The rms noise on the resulting map is ~ 6 mJy/beam km/s. The contours go from 0.1 to 8 in steps of 0.7 Jy/beam km/s. The crosses mark the positions of the two dense cores. The alma beam is represented as a yellow elliptical symbol on the bottom right corner of the image. We can see the excellent match between the Spitzer dust extinction of the filaments and the $N_2H^+(1-0)$ emission; (c) ALMA $N_2H^+(1-0)$ velocity field using the 1st order moment map. The crosses mark the positions of the cores and the contours are the same as in the (b) panel.

bulk of the cloud. Such line profiles are expected for an optically thick tracer of idealized collapsing clouds in which the excitation temperature is rising towards the centre. What is important to note here is the extent (over at least 12 independent Mopra beams) over which this spectral signature is observed, and also the absence of any other line asymmetry. For instance, for expanding motions we would expect red-shifted self-absorbed spectra, while in the case of rotation blue-shifted and red-shifted spectra on either side of the rotation axis should be produced. Therefore these $HCO^+(1-0)$ observations towards SDC335 already rule out the possibility of rotating or expanding cloud, and strongly suggest that SDC335 is collapsing. SDC335 is well enough characterised that we can estimate the opacity of the central $HCO^+(1-0)$ line using the 1D non-LTE RADEX radiative transfer code (?). This code predicts line intensities based on a set of input parameters for which we have strong constraints: the kinetic temperature (20 ± 5 K; cf Appendix A), the cosmic background temperature (2.73 K), the central H_2 density averaged over the Mopra beam ($6 \pm 1 \times 10^4$ cm $^{-3}$, estimated from the column density map presented in Fig. 1), and the velocity dispersion (1.3 ± 0.3 km/s; cf Sect. 5.3). Then we iterate on the last input parameter, i.e. the molecule column density, in order to match the model line intensities with the observed line temperature, i.e. $T_{HCO^+}^{peak} = 6.4(\pm 0.2)$ K in T_{mb} scale. Doing so we obtain $N_{HCO^+} = 6_{-3}^{+7} \times 10^{13}$ cm $^{-2}$, corresponding to an abundance $X_{HCO^+} = 7_{-4}^{+8} \times 10^{-10}$. The corresponding opacities and excitation temperatures are $\tau_{HCO^+} = 2.8_{-1.2}^{+2.8}$ and $T_{ex} = 10.4_{-0.7}^{+1.2}$ K. These calculations confirm that $HCO^+(1-0)$ is optically thick in SDC335 and that it is not thermalised. Using the same set of parameters we performed the same exercise of the central $H^{13}CO^+(1-0)$ line (see Fig. C.1) which has $T_{H^{13}CO^+}^{peak} = 1.2(\pm 0.2)$ K in T_{mb} scale. For this line we obtain $N_{H^{13}CO^+} = 4_{-2}^{+3} \times 10^{12}$ cm $^{-2}$, corresponding to an abundance $X_{H^{13}CO^+} = 5_{-3}^{+3} \times 10^{-11}$. The corresponding opacities and excitation temperatures are $\tau_{H^{13}CO^+} = 0.4_{-0.1}^{+0.2}$ and $T_{ex} = 6.5_{-1.2}^{+2.7}$ K. Therefore, as for $HCO^+(1-0)$, $H^{13}CO^+(1-0)$

is not thermalised but is marginally optically thin. Another important to make here is the fact that given the abundances we calculated for both molecules, we obtain an abundance ratio $15 \leq [HCO^+]/[H^{13}CO^+] \leq 20$. The $[^{12}C]/[^{13}C]$ is known to increase as a function of the galactocentric radius, and at the galactocentric distance of SDC335 (i.e. ~ 5 kpc) the predicted $[^{12}C]/[^{13}C]$ is around 30 (Langer & Penzias 1993; Savage et al. 2002). The value we find is twice as much, which is, considering the uncertainties on these kind of measurements, in reasonable agreement. We will use the latter value of the fractional abundance for the radiative modelling presented in Sect. 5.3.

4.3. ALMA $N_2H^+(1-0)$ cloud velocity field

Figure 4b shows the ALMA $N_2H^+(1-0)$ integrated intensity map of SDC335. The visual comparison with the *Spitzer* image of SDC335 demonstrates how efficient this molecule is in tracing the network of pc-long filaments seen in dust extinction. This justifies our choice to use this line to trace the filaments kinematics. On the other hand, we can also see that N_2H^+ is not an optimal tracer of the cores, where the central heating may have partly removed it from the gas phase (Zinchenko et al. 2009; Busquet et al. 2011).

Figures 4c and 5 show that SDC335 velocity field is homogeneous in each filament, with distinct velocities from filament to filament (e.g. $\langle V_{F1} \rangle = -47.4 \pm 0.1$ km/s; $\langle V_{F3} \rangle = -45.8 \pm 0.2$ km/s). It becomes more complex towards the centre of the cloud. On Fig. 5 we see that two separate velocity components are present close to MM2, while the broad asymmetric line profiles around MM1 suggest their blending, consistent with observations of other massive cores (Csengeri et al. 2011). This line shape cannot be the result of large optical depth since the $N_2H^+(1-0)$ hyperfine line fitting (performed with GILDAS) gives an opacity lower than 1 everywhere in the cloud. Kinetically, the gas traced by $N_2H^+(1-0)$ at the centre of the cloud is composed of a mix of the gas originating from the two main filaments, F1 and F2. Figure 5 (right) presents a schematic view

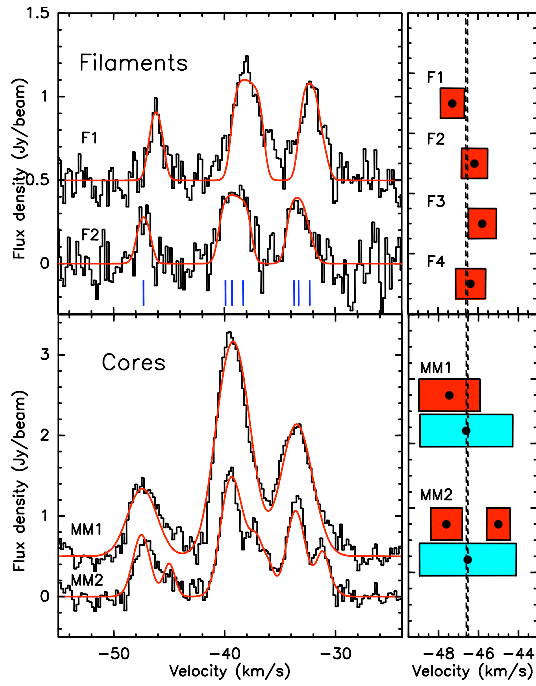


Fig. 5. (left) Examples of combined ALMA and Mopra $N_2H^+(1-0)$ spectra observed at some specific positions in SDC335, along with their best fits as red solid lines. The $N_2H^+(1-0)$ spectra exhibit a hyperfine structure (HFS) composed of 7 components (which positions are displayed as blue vertical ticks for the F2 filament). Some of these components are close enough to be blended when the velocity dispersion of the gas is supersonic, resulting in three groups of lines. For a kinetic temperature of 10K, the velocity dispersion along the filaments is supersonic by a factor 1.5 to 3, similar to what has been observed in other IRDCs (Ragan et al. 2012). (right) Schematic representation of the systemic velocity and velocity dispersion of the different structures. The length of the boxes represents their velocity dispersion (FWHM) of the gas, and its central position their systemic velocity (represented as a filled circle). The colour of the boxes codes the line which has been used for the measurements: red for $N_2H^+(1-0)$, and cyan for $CH_3OH(13-12)$. The vertical dashed lines mark the systemic velocities of the cores.

of the velocities of the filaments and cores. We can actually see that the two cores lie at an intermediate velocity between the velocities of the different filaments. Such a configuration suggests that the cores are at least partly fed by the pristine gas flowing along these filaments at a velocity $V_{inf} \simeq 1$ km/s.

5. Discussion

5.1. SDC335: An OB cluster progenitor

In Section 3 we inferred core masses such as $M_{MM1} = 545^{+770}_{-385} M_\odot$ and $M_{MM2} = 65^{+92}_{-46} M_\odot$ in deconvolved diameters $0.05 - 0.06$ pc. These values place MM1 as one of the most massive protostellar cores ever observed in the Galaxy. To better appreciate this, Fig. 6 shows a radius versus mass diagram for a significant (but not complete) sample of massive protostellar cores published in the literature. On this diagram we can clearly see that SDC335 MM1 stands out, and for cores with similar sizes MM1 is a factor of 3 up to a factor of 20 more massive. However, given the uncertainties on the dust properties and density profile profile of cores, MM1 could match the mass of the most massive cores observed, on smaller scales, in Cygnus X (Bontemps et al. 2010).

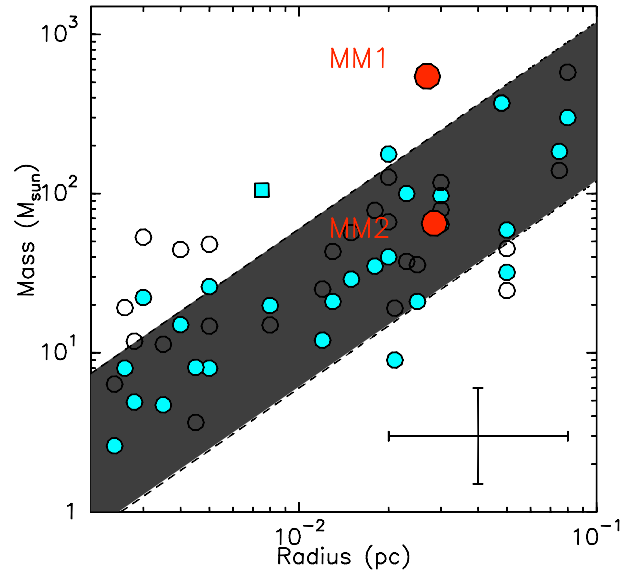


Fig. 6. Mass-radius diagram of massive protostellar cores. The cyan circles correspond to the values as published in the literature (Peretto et al. 2007; Ren et al. 2012; Rathborne et al. 2011; Wang et al. 2011; Zhang & Wang 2011; Bontemps et al. 2010; Rathborne et al. 2007, 2008; Beuther et al. 2002, 2003, 2005, 2012; Molinari et al. 1998; Rodón et al. 2012), while the empty circles correspond to the same set of sources for which we recalculated the mass using the same dust opacity law as in this paper. The MM1 and MM2 sources are indicated as red filled circles. The cyan filled square marks the position of the W51 North star+disc system from Zapata et al. (2009). The shaded area indicates the region where most sources lie. The cross in the bottom right corner indicates a factor of 2 uncertainty in both the masses and sizes, typical of the results presented here.

Another interesting source to compare with is W51 North. This source is believed to contain an already formed $\geq 65 M_\odot$ star, with a surrounding 3000 AU accreting disc of $40 M_\odot$ (Zapata et al. 2009). When adding up this source (star+disc) on the mass-radius diagram of Fig. 6 we indeed see that W51 North is also extreme. SDC335 MM1 could represent an earlier version of such O-type star forming system. For compact cores, the fraction of mass likely to be accreted onto the star is typically 50% of the total core mass (McKee & Tan 2003, Duarte-Cabral et al., *subm.*). Despite probable unresolved fragmentation on smaller scales, the MM1 core and its large mass have the potential to form at least one star of $50 M_\odot$ to $100 M_\odot$.

Assuming **now that within SDC335 ($M = 5500 \pm 800 M_\odot$) a fully sampled standard Initial Mass Function forms** (Kroupa 2002; Chabrier 2003), **then, in addition to the early O-type star in MM1, a $\sim 1000 M_\odot$ cluster of ~ 320 stars with masses from 1 to $50 M_\odot$ should emerged from SDC335.** Including lower mass stars in this calculation we would reach a star formation efficiency $\geq 50\%$, the necessary condition to form an open bound cluster (e.g. Lada & Lada 2003). As a whole, SDC335 could potentially form an OB cluster similar to the Trapezium cluster in Orion (Zinnecker & Yorke 2007).

5.2. A large mass reservoir for MM1

We can estimate the conditions under which MM1 formed within the context of gravo-turbulent fragmentation models. Using standard (lognormal) volume density Probability Density Function (PDF) of non self-gravitating turbulent clouds (e.g. Padoan et al. 1997; Hennebelle & Chabrier 2008), we calculate (see Ap-

pendix) that less than 0.01% of the gas is expected to be above a density of 10^7 cm^{-3} , while $> 10\%$ of the SDC335 mass is above this threshold in the form of cores (see Table 1). Therefore, gravity must have brought together such a large mass in such a small volume. A first possibility is that the material lying currently in MM1 was initially part of a larger volume which then collapsed. To calculate the diameter D_{ini} of this volume we first need to calculate the density ρ_{ini} above which 10% of the gas is lying assuming a lognormal density PDF. Using the observed parameters of SDC335 (see Appendix A) we find that D_{ini} of this initial volume must have been ~ 15 times larger than the current MM1 size, which means $D_{ini} \sim 0.8 \text{ pc}$. This size is in fact a lower limit since the calculation implicitly assumes that all the dense gas above ρ_{ini} lies within a single over-density. The second possibility is that MM1 initially had the same diameter as observed today. It is then possible to calculate the maximum mass that volume can contain in order to match the lognormal PDF. We can show (see Appendix A) that the maximum initial mass of such a core is $\sim 3 M_{\odot}$. This low mass means that most of the current MM1 mass must have been accreted from its surroundings. Using the current average density of SDC335 we calculate that the region from which MM1 accreted matter would have to have a diameter of 1.2 pc. Either of these scenarios, therefore, requires large-scale, rather than local, accretion/collapse to form MM1.

5.3. Collapse on large-scale

The Mopra $\text{HCO}^+(1-0)$ spectra presented in Fig. 3 are suggestive of global gravitational collapse. A simple analytical model (Myers et al. 1996) allows to get a first guess to the infall velocity from such spectra based on the line characteristics. Using this model we obtain an infall velocity of $\sim 0.4 \text{ km/s}$. However, as noted by De Vries & Myers (2005) this model underestimates the infall velocity by a factor of ~ 2 . We therefore decided to run a more sophisticated radiative transfer model to better constrain this infall velocity. For this purpose we used the RATRAN 1D Monte Carlo radiative transfer code (Hogerheijde & van der Tak 2000). The input parameters for the calculations are the mass of the cloud, its radius, density profile, kinetic temperature profile, turbulent velocity dispersion, the infall velocity profile and abundance profile of the line to be modelled. Obviously, a 1D model cannot describe the detailed kinematics of the filamentary structures observed in SDC335, and for this reason we decided to model only the central $\text{HCO}^+(1-0)$ and $\text{H}^{13}\text{CO}^+(1-0)$ spectra. We used the SDC335 mass and size quoted in Table 1, a cloud density profile such as $\rho \propto r^{-1.5}$ and a constant temperature profile of 20 K. Based on the discussion in Sec. 4.2 we fixed the HCO^+ abundance (relative to H_2) to 7×10^{-10} and an abundance ratio $[\text{HCO}^+]/[\text{H}^{13}\text{CO}^+]$ of 30. We then ran a grid of models varying the last two input parameters, i.e., the infall velocity and the velocity dispersion. Figure 7 shows the results of the $\text{HCO}^+(1-0)$ modelling of the central pixel for infall velocities ranging from 0.4 km/s to 0.9 km/s, and velocity dispersions from 0.8 km/s to 1.2 km/s. The corresponding $\text{H}^{13}\text{CO}^+(1-0)$ modellings are displayed in Appendix C. From Fig. 7 we consider that $0.5 \text{ km/s} \leq V_{inf} \leq 0.9 \text{ km/s}$ and $0.8 \text{ km/s} \leq \sigma_{turb} \leq 1 \text{ km/s}$ provide reasonable fits to the central $\text{HCO}^+(1-0)$ spectrum. We also performed models varying the radius of the collapsing region R_{inf} . For $R_{inf} < 0.5 \text{ pc}$ the modelled $\text{HCO}^+(1-0)$ spectra remain symmetric, which is inconsistent with the observations. Only from $R_{inf} \geq 0.8 \text{ pc}$ the asymmetry is large enough to resemble the observed one.

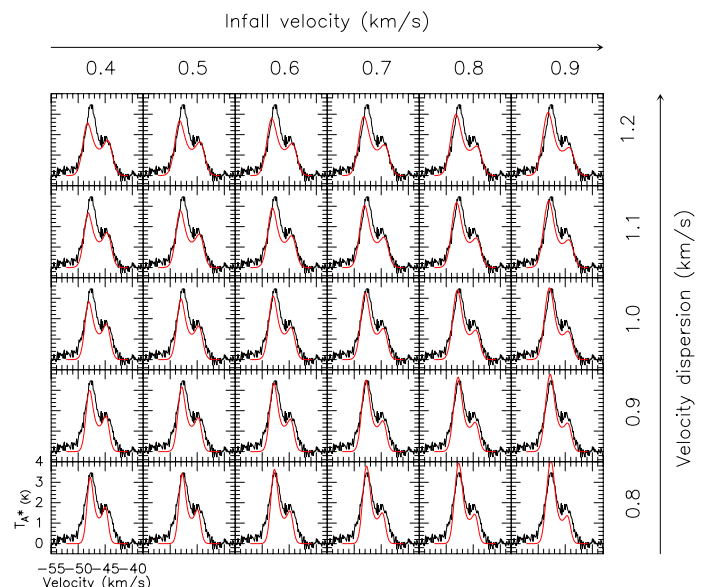


Fig. 7. Grid of $\text{HCO}^+(1-0)$ spectra obtained from RATRAN modelling of a collapsing cloud (see text). All input parameters are fixed with the exception of the infall velocity (V_{inf}) and velocity dispersion (σ_{turb}). Each modelled spectrum (in red) has been obtained for the corresponding $V_{inf} - \sigma_{turb}$ displayed on the top and right hand sides of the figure. The $\text{HCO}^+(1-0)$ spectrum observed at the centre of SDC335 is in black. Since we wanted to keep the observed spectra displayed in T_a scale, we applied a 0.5 factor to the modelled spectra in order to take into account the main beam efficiency.

This shows that the observed $\text{HCO}^+(1-0)$ self-absorbed spectra towards SDC335 do trace global collapse.

5.4. Energy balance

To be collapsing, the gravitational energy of a cloud has to overcome the kinetic energy that supports it. That is if the virial parameter $\alpha_{vir} = 5\sigma_{turb}^2 R / (GM)$ is less than 1 (Bertoldi & McKee 1992). In this equation σ_{turb} , R and M are the 1D velocity dispersion, the cloud radius and the cloud gas mass. In the case of SDC335, we estimated $\sigma_{turb} = 1.3 \text{ km/s}$ from the averaged $\text{N}_2\text{H}^+(1-0)$ spectrum over SDC335 as observed with Mopra. Using Mopra $^{13}\text{CO}(1-0)$ data (not discussed in this paper), which traces less dense gas, we obtained $\sigma_{turb} = 1.6 \text{ km/s}$. Note also that these velocity dispersion measurements include any systematic motions within the beam, such as infall, which artificially increase the velocity dispersion estimate (Peretto et al. 2007). Taking this into account and given the fact that the filaments are well traced by N_2H^+ we estimate $\sigma_{turb} = 1.3(\pm 0.3) \text{ km/s}$. With $R = 1.2 \text{ pc}$ and $M = 5500(\pm 800) M_{\odot}$ we find $\alpha_{vir} = 0.4^{+0.4}_{-0.2} < 1$. Additional support against gravity could be provided by magnetic field. Following earlier studies (Pillai et al. 2011), we estimate that the magnetic field strength $|B|_{vir}$ necessary to virialize SDC335 is $|B|_{vir} = 300 \mu\text{G}$, which is at least 3 times higher than observations of clouds at similar densities suggest (Crutcher 2012). Finally, note that support from centrifugal forces can potentially stabilise a cloud against gravity. However, calculating the rotational energy of SDC335 by assuming that it is a homogenous rotating sphere with an angular velocity $\omega = 1 \text{ km/s/pc}$, we estimate that it is ~ 10 times smaller than its kinetic energy. In other words, it is negligible.

5.5. Large-scale velocity field and accretion rates

In order to illustrate some of the expected signatures of globally collapsing clouds we present, in Fig. 8, a snapshot of a published MHD simulation modelling the evolution of a turbulent and magnetized $10\,000\ M_{\odot}$ cloud, and initially designed to reproduce some of the observational signatures of the DR21 region (Schneider et al. 2010, and see Appendix D for more details on the simulation). Overall this simulation shows some similarities with SDC335, i.e. presence of massive cores in the centre, the formation of filaments converging towards these cores, and a velocity field resembling the one observed in SDC335 (see Fig. 4c). But most importantly, Fig. 8 shows that if a fraction of the gas is indeed collapsing along the filaments, a large fraction is collapsing off filaments. In such a case the filamentary accretion observed along the filaments represents only the tip of the entire accretion towards the cloud centre.

In the context of a global collapse scenario, the observed velocity field along the filaments is the consequence of the inflowing cold gas. We can therefore estimate the current infall rate of gas running through the filaments using $\dot{M}_{inf} = N_{fil}\pi R_{fil}^2 V_{inf}\rho_{fil}$, where N_{fil} is the number of filaments, R_{fil} is the filament cross-section radius, V_{inf} is the gas infall velocity and ρ_{fil} is the gas volume density. With 6 filaments, an infall velocity of $0.7(\pm 0.2)$ km/s, a filament section radius of 0.15 pc, and a density of $4(\pm 1) \times 10^4\ \text{cm}^{-3}$, we get an infall rate of $0.7(\pm 0.3) \times 10^{-3}\ M_{\odot}/\text{yr}$. At this rate, a total mass of $210(\pm 90)\ M_{\odot}$ would have been gathered in the centre by filamentary accretion within a free-fall time of $\sim 3 \times 10^5$ yr. This is slightly less than half of the cumulated core masses. However, less than 20% of the SDC335 mass is lying within the filaments (cf Section 3). Assuming that the remaining gas is collapsing off filaments at a similar infall velocity, as it is observed in the simulations (see Fig. 8a), the total accretion rate becomes $\dot{M}_{inf} = 4\pi R_{sph}^2 V_{inf}\rho_{sph}$ where R_{sph} is the radius of the considered spherical volume and ρ_{sph} is the density at that radius. At the radius of the Centre region, $R_{sph} = 0.6$ pc and $\rho_{sph} = 1.3(\pm 0.2) \times 10^4\ \text{cm}^{-3}$, which leads to $\dot{M}_{inf} = 2.5(\pm 1.0) \times 10^{-3}\ M_{\odot}/\text{yr}$. With such an accretion rate $750(\pm 300)\ M_{\odot}$ of pristine gas is trapped inside the Centre region every cloud free-fall time. This is enough to double the mass of material currently present in the Centre region in $3.5^{+2.2}_{-1.0}$ cloud free-fall times. Altogether, evidence indicates that, if not all, a significant fraction of the SDC335 core masses could have been built through the parsec-scale collapse of their parental cloud.

6. Summary and conclusion

SDC335 is a massive ($5500 \pm 800\ M_{\odot}$) IRDC with two massive star forming cores located in its centre, one of which is likely to be an early O-type star progenitor. This core has an estimated mass of $545^{+770}_{-385}\ M_{\odot}$ in a deconvolved diameter of ~ 0.05 pc, which makes it one of the most massive protostellar cores ever observed in the Galaxy. A theoretical argument based on volume density PDFs of molecular clouds suggests that such a concentration of mass must occur through the large scale collapse of the surrounding cloud. This scenario is supported by several observational facts presented in this paper: optically thick molecular line observations showing extended collapse signatures; virial parameter significantly lower than 1; velocity field consistent with the one obtained from models of globally collapsing molecular clouds; accretion rates which are large enough to provide an additional $750(\pm 300)\ M_{\odot}$ of pristine gas to the central

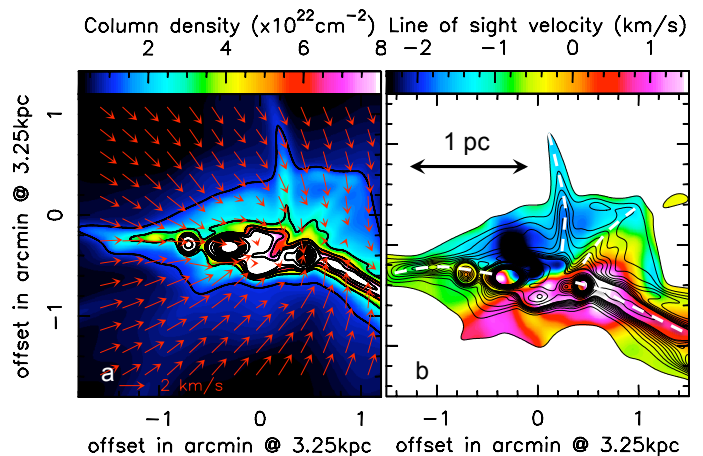


Fig. 8. Snapshot of a MHD simulation of a $10\,000\ M_{\odot}$ collapsing cloud (see Appendix for more details; Schneider et al. 2010). (a) Column density (colour and contours) smoothed to the resolution of the ALMA data ($5''$). The arrows show the plane of the sky velocity field. We see that gas flows along filaments and also off the filaments. (b) Dense gas line-of-sight velocity field (colour scale) smoothed to the resolution of the ALMA data. We emphasized the presence of filaments by white dashed lines. The contours are the same as in panel (a).

pc-size region of SDC335 per cloud free-fall time. Altogether, these observations strongly suggest that the SDC335 massive star forming cores managed to build-up their large masses thanks to the supersonic global collapse of their surrounding cloud. **Even though it still remains to be demonstrated that global collapse is the main process through which massive star progenitors accumulate mass, the case of SDC335 sets strong constraints on any theory of massive star formation.**

Acknowledgements. NP was supported by a CEA/Marie Curie Eurotalents fellowship and benefited from the support of the European Research Council advanced grant ORISTARS (Grant Agreement no. 291294). ADC was supported by the PROBEs project funded by the French National Research Agency (ANR). JEP has received funding from the European Community Seventh Framework Programme (FP7/2007-2013) under grant agreement No. 229517. We also acknowledge the support of the European ALMA Regional Centre (ARC) and the UK ARC node. This paper makes use of the following ALMA data: ADS/JAO.ALMA#2011.0.00474.S. ALMA is a partnership of ESO (representing its member states), NFS (USA) and NINS (Japan), together with NRC (Canada) and NSC and ASIAA (Taiwan), in cooperation with the Republic of Chile. The Joint ALMA Observatory is operated by ESO, AUI/NRAO and NAOJ. The Mopra radio telescope is part of the Australia Telescope National Facility which is funded by the Commonwealth of Australia for operation as a National Facility managed by CSIRO. The University of New South Wales Digital Filter Bank used for the observations with the Mopra telescope was provided with the support from Australian Research Council.

References

- André, P., Men'shchikov, A., Bontemps, S., et al. 2010, *A&A*, 518, L102+
 Beckwith, S. V. W., Sargent, A. I., Chini, R. S., & Guesten, R. 1990, *AJ*, 99, 924
 Bertoldi, F. & McKee, C. F. 1992, *ApJ*, 395, 140
 Beuther, H., Churchwell, E. B., McKee, C. F., & Tan, J. C. 2007, *Protostars and Planets V*, 165
 Beuther, H. & Schilke, P. 2004, *Science*, 303, 1167
 Beuther, H., Schilke, P., Gueth, F., et al. 2002, *A&A*, 387, 931
 Beuther, H., Schilke, P., & Stanke, T. 2003, *A&A*, 408, 601
 Beuther, H., Sridharan, T. K., & Saito, M. 2005, *ApJ*, 634, L185
 Beuther, H., Tackenberg, J., Linz, H., et al. 2012, *A&A*, 538, A11
 Bonnell, I. A., Vine, S. G., & Bate, M. R. 2004, *MNRAS*, 349, 735
 Bontemps, S., Motte, F., Csengeri, T., & Schneider, N. 2010, *A&A*, 524, A18
 Busquet, G., Estalella, R., Zhang, Q., et al. 2011, *A&A*, 525, A141
 Butler, M. J. & Tan, J. C. 2009, *ApJ*, 696, 484
 Caswell, J. L., Fuller, G. A., Green, J. A., et al. 2011, *MNRAS*, 417, 1964
 Chabrier, G. 2003, in *IAU Symposium*, Vol. 221, *IAU Symposium*, 67P+

- Churchwell, E., Babler, B. L., Meade, M. R., et al. 2009, *PASP*, 121, 213
 Crutcher, R. M. 2012, *ARA&A*, 50, 29
 Csengeri, T., Bontemps, S., Schneider, N., et al. 2011, *ApJ*, 740, L5
 Cyganowski, C. J., Brogan, C. L., Hunter, T. R., & Churchwell, E. 2011, *ApJ*, 743, 56
 Cyganowski, C. J., Whitney, B. A., Holden, E., et al. 2008, *AJ*, 136, 2391
 De Vries, C. H. & Myers, P. C. 2005, *ApJ*, 620, 800
 Fuller, G. A., Williams, S. J., & Sridharan, T. K. 2005, *A&A*, 442, 949
 Garay, G., Brooks, K. J., Mardones, D., Norris, R. P., & Burton, M. G. 2002, *ApJ*, 579, 678
 Griffin, M. J., Abergel, A., Abreu, A., et al. 2010, *A&A*, 518, L3+
 Hennebelle, P. & Chabrier, G. 2008, *ApJ*, 684, 395
 Hennemann, M., Motte, F., , N., et al. 2012, *A&A*, 543, L3
 Hildebrand, R. H. 1983, *QJRAS*, 24, 267
 Hoare, M. G. 2005, *Ap&SS*, 295, 203
 Hogerheijde, M. R. & van der Tak, F. F. S. 2000, *A&A*, 362, 697
 Kauffmann, J. & Pillai, T. 2010, *ApJ*, 723, L7
 Kroupa, P. 2002, *Science*, 295, 82
 Lada, C. J. & Lada, E. A. 2003, *ARA&A*, 41, 57
 Langer, W. D. & Penzias, A. A. 1993, *ApJ*, 408, 539
 McKee, C. F. & Tan, J. C. 2003, *ApJ*, 585, 850
 McMullin, J. P., Waters, B., Schiebel, D., Young, W., & Golap, K. 2007, in *Astronomical Society of the Pacific Conference Series*, Vol. 376, *Astronomical Data Analysis Software and Systems XVI*, ed. R. A. Shaw, F. Hill, & D. J. Bell, 127
 Molinari, S., Swinyard, B., Bally, J., et al. 2010, *A&A*, 518, L100+
 Molinari, S., Testi, L., Brand, J., Cesaroni, R., & Palla, F. 1998, *ApJ*, 505, L39
 Myers, P. C. 2009, *ApJ*, 700, 1609
 Myers, P. C., Mardones, D., Tafalla, M., Williams, J. P., & Wilner, D. J. 1996, *ApJ*, 465, L133
 Padoan, P., Nordlund, A., & Jones, B. J. T. 1997, *MNRAS*, 288, 145
 Paradis, D., Veneziani, M., Noriega-Crespo, A., et al. 2010, *A&A*, 520, L8
 Peretto, N., André, P., & Belloche, A. 2006, *A&A*, 445, 979
 Peretto, N., André, P., Könyves, V., et al. 2012, *A&A*, 541, A63
 Peretto, N. & Fuller, G. A. 2009, *A&A*, 505, 405
 Peretto, N. & Fuller, G. A. 2010, *ApJ*, 723, 555
 Peretto, N., Fuller, G. A., Plume, R., et al. 2010, *A&A*, 518, L98+
 Peretto, N., Hennebelle, P., & André, P. 2007, *A&A*, 464, 983
 Pilbratt, G. L., Riedinger, J. R., Passvogel, T., et al. 2010, *A&A*, 518, L1+
 Pillai, T., Kauffmann, J., Wyrowski, F., et al. 2011, *A&A*, 530, A118
 Poglitsch, A., Waelkens, C., Geis, N., et al. 2010, *A&A*, 518, L2+
 Ragan, S. E., Heitsch, F., Bergin, E. A., & Wilner, D. 2012, *ApJ*, 746, 174
 Rathborne, J. M., Garay, G., Jackson, J. M., et al. 2011, *ApJ*, 741, 120
 Rathborne, J. M., Jackson, J. M., & Simon, R. 2006, *ApJ*, 641, 389
 Rathborne, J. M., Jackson, J. M., Zhang, Q., & Simon, R. 2008, *ApJ*, 689, 1141
 Rathborne, J. M., Simon, R., & Jackson, J. M. 2007, *ApJ*, 662, 1082
 Reid, M. J., Menten, K. M., Zheng, X. W., et al. 2009, *ApJ*, 700, 137
 Ren, Z., Wu, Y., Zhu, M., et al. 2012, *MNRAS*, 422, 1098
 Rodón, J. A., Beuther, H., & Schilke, P. 2012, *A&A*, 545, A51
 Savage, C., Apponi, A. J., Ziurys, L. M., & Wyckoff, S. 2002, *ApJ*, 578, 211
 Schneider, N., Csengeri, T., Bontemps, S., et al. 2010, *A&A*, 520, A49
 Schneider, N., Csengeri, T., Hennemann, M., et al. 2012, *A&A*, 540, L11
 Smith, R. J., Longmore, S., & Bonnell, I. 2009, *MNRAS*, 400, 1775
 Smith, R. J., Shetty, R., Stutz, A. M., & Klessen, R. S. 2012, *ApJ*, 750, 64
 Traficante, A., Calzoletti, L., Veneziani, M., et al. 2011, *MNRAS*, 416, 2932
 Wang, K., Zhang, Q., Wu, Y., & Zhang, H. 2011, *ApJ*, 735, 64
 Wilcock, L. A., Ward-Thompson, D., Kirk, J. M., et al. 2012, *MNRAS*, 424, 716
 Xu, Y., Li, J. J., Hachisuka, K., et al. 2008, *A&A*, 485, 729
 Zapata, L. A., Ho, P. T. P., Schilke, P., et al. 2009, *ApJ*, 698, 1422
 Zhang, Q. & Wang, K. 2011, *ApJ*, 733, 26
 Zinchenko, I., Caselli, P., & Pirogov, L. 2009, *MNRAS*, 395, 2234
 Zinnecker, H. & Yorke, H. W. 2007, *ARA&A*, 45, 481

Appendix A: *Herschel* dust temperature map

Along with the *Herschel* column density map presented in Fig. 1 we constructed a dust temperature map shown in Fig. A.1 (see Sect. 3.1 for more details). On this image we see that the two protostellar cores are warming up the central region up to 21 K while it reaches 16 K in the coldest parts of SDC335. Some artefacts are actually visible on this image. Indeed, the temperature peaks are shifted with respect to the position of the cores. Using a 350 μ m SABOCA image of SDC335 (Pineda et al. in prep.) we have been able to associate these shifts to some artefacts in the *Herschel* 350 μ m image. Indeed, as already mentioned, the *Herschel* 250 μ m image is saturated towards MM1 and, even though not saturated, the 350 μ m *Herschel* PSF is clearly affected at the position of MM1. However, comparing the column density and temperature maps obtained with SABOCA with the ones presented here we are confident that, overall, the physical quantities are barely affected.

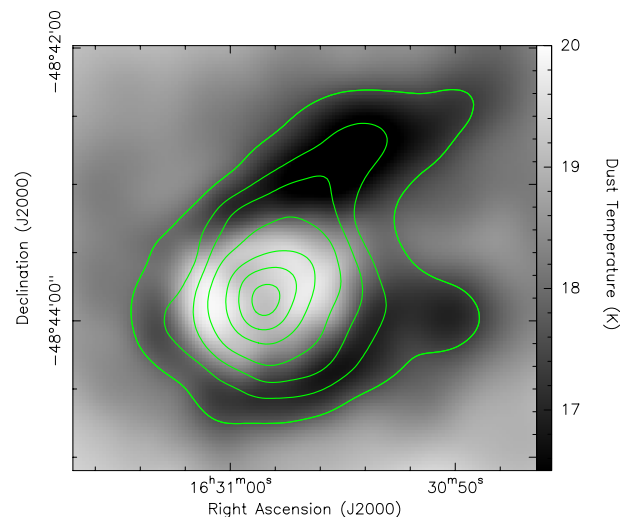


Fig. A.1. SDC335 *Herschel* dust temperature map. The contours are the same column density contours as in Fig. 1.

Appendix B: Volume density PDF calculations

Volume density PDFs of turbulent, non self-gravitating molecular clouds can be described as a lognormal function of the logarithmic density contrast $\delta = \log(\rho/\bar{\rho})$ (Padoan et al. 1997; Hennebelle & Chabrier 2008):

$$\mathcal{P}(\delta) = \frac{1}{\sqrt{2\pi\sigma_0^2}} \exp\left[-\frac{(\delta - \bar{\delta})^2}{2\sigma_0^2}\right] \quad (\text{B.1})$$

where σ_0 is the standard deviation of the distribution, and $\bar{\delta} = -\sigma_0^2/2$. Furthermore, the standard deviation of this PDF can be written as $\sigma_0^2 = \ln(1 + bM^2)$ where M is the Mach number and $b \approx 0.25$.

Integrating Equation (A.1) we can estimate what fraction of a cloud is supposed to lie above a certain density threshold, ρ_{th} , before gravity takes over. Setting the two free parameters of Eq. A.1 to the SDC335 observed values ($\bar{\rho} = 1.3 \times 10^4 \text{ cm}^{-3}$ and $M = 6$) we find that less than 0.01% of the gas should lie above $\rho_{th} = 1 \times 10^7 \text{ cm}^{-3}$. This is more than 3 orders of magnitude difference with what is observed in SDC335.

Now we can estimate the density ρ_{ini} (and $\delta_{ini} = \rho_{ini}/\bar{\rho}$) at which the following relation is fulfilled:

$$\frac{M_{MM1}}{M_{SDC335}} = \int_{\delta_{ini}}^{\infty} \mathcal{P}(\delta) d\delta \quad (\text{B.2})$$

which is equivalent to:

$$0.1 = 0.5 \times (1 - \text{erf}[(\delta_{ini} - \bar{\delta})/\sqrt{2\sigma_0^2}]) \quad (\text{B.3})$$

Doing so we find $\rho_{ini} = 3.5 \times 10^4 \text{ cm}^{-3}$. Then we can calculate the volume diameter in which the MM1 mass was initially contained using $D_{ini} = 2 \times [3M_{MM1}/(4\pi\rho_{ini})]^{1/3} = 0.8 \text{ pc}$. Note that here we used ρ_{ini} as the mean density of the initial volume while it formally is the minimum density within the volume under consideration. The true mean density is necessarily larger, although it cannot be too centrally concentrated either since it would not satisfy the volume density PDF. It is therefore reasonable to use ρ_{ini} as the mean density, especially that the dependency of D_{ini} in ρ_{ini} is weak.

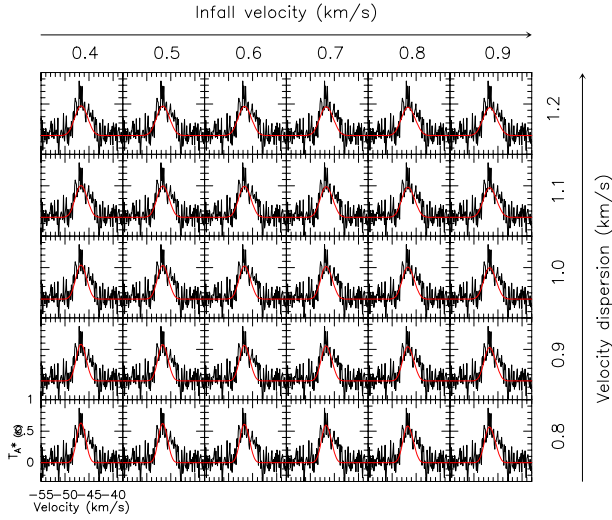


Fig. C.1. Same as Fig. 7 but for the $\text{H}^{13}\text{CO}^+(1-0)$ line.

Finally, we can estimate what is the maximum M_{ini} one can have in the current MM1 volume which satisfies the volume density PDF, such as:

$$\frac{M_{ini}}{M_{S\text{DC}335}} = \int_{\delta_{ini}}^{\infty} \mathcal{P}(\delta) d\delta \quad (\text{B.4})$$

with $M_{ini} = \rho_{ini} V_{MM1}$. We find that $M_{ini} \approx 3 M_{\odot}$ which means that in this case nearly all MM1 mass must come from its surrounding. We can estimate the volume of this surrounding by taking $D_{ini} = 2 \times [3M_{MM1}/(4\pi\bar{\rho})]^{1/3} = 1.2 \text{ pc}$.

Appendix C: $\text{H}^{13}\text{CO}^+(1-0)$ RATRAN modelling

Figure C.1 presents the optically thin $\text{H}^{13}\text{CO}^+(1-0)$ modelled spectra obtain with RATRAN for the cloud collapse model discussed in Sec. 5.3. We see that the modelled lines overall match quite well the observed spectrum even though, in nearly all cases, the modelled one is a bit too narrow. This can potentially be explained by a more complex infall profile than the one we used for these calculation, resulting in a slightly broader line. The fact that the modelled spectra have peak temperatures close to the observed one comforts our choice of HCO^+ and H^{13}CO^+ abundances.

Appendix D: Additional details on the MHD simulation

The simulation presented in this study (Fig. 8 of the paper) were initially performed to model the DR21 region (Schneider et al. 2010). It is a MHD simulation of a self-gravitating cloud performed with the AMR RAMSES code. The initial conditions of the simulation consisted of a $10\,000 M_{sun}$ ellipsoidal cloud, with an aspect ratio of 2, and a density profile as $\rho(r, z) = \rho_0/[1 + (r/r_0)^2 + (z/z_0)^2]$, where $r = \sqrt{(x^2 + y^2)}$, $z_0 = 2r_0$, $r_0 = 5 \text{ pc}$, and $\rho_0 = 500 \text{ cm}^{-3}$. The density at the edge of the cloud is $\rho_{edge} = 50 \text{ cm}^{-3}$, and is maintained in pressure equilibrium with an external medium at lower density. The magnetic field is perpendicular to the main axis of the cloud, with an intensity proportional to the cloud column density and a peak value of $7 \mu\text{G}$. By the time of the snapshot presented in this paper, the magnetic field had increased to $\sim 100 \mu\text{G}$ in the densest

regions, with an average value over the dense gas of $\sim 20 \mu\text{G}$. The simulation is isothermal at a temperature of 10 K. A turbulent velocity field was seeded to initially get, over the entire cloud, $2T + W + M \approx 0$ where T is the kinetic energy (thermal and turbulent), W the gravitational energy, and M the magnetic energy. Turbulence was undriven and allowed to decay. These conditions lead to $W \approx 2T \approx 9M$. Despite the fact that, globally, the turbulent and magnetic energy compensate the gravitational energy of the cloud, it quickly becomes sub-virial due to the compressive nature of turbulence and the fact that its energy quickly dissipates. The consequence of this is the fragmentation and global collapse of the simulated cloud.